Journal of Computational and Applied Mathematics 270 (2014) 330–342

Contents lists available at ScienceDirect

Journal of Computational and Applied Mathematics

journal homepage: www.elsevier.com/locate/cam

A parallel non-conforming multi-element DGTD method for the simulation of electromagnetic wave interaction with metallic nanoparticles

Raphaël Léger [b,*], Jonathan Viquerat [b], Clément Durochat [b], Claire Scheid [a,b], Stéphane Lanteri [b]

[a] University of Nice - Sophia Antipolis, J.A. Dieudonné Mathematics Laboratory UMR CNRS 7351, 06108 Nice Cedex 02, France
[b] INRIA Sophia Antipolis-Méditerranée research center, Nachos project-team, 06902 Sophia Antipolis Cedex, France

ARTICLE INFO

Article history:
Received 27 September 2013
Received in revised form 17 December 2013

Keywords:
Maxwell equations
Dispersive media
Discontinuous Galerkin method
Non-conforming multi-element mesh
Parallel computing

ABSTRACT

The present work is about the development of a parallel non-conforming multi-element discontinuous Galerkin time-domain (DGTD) method for the simulation of the scattering of electromagnetic waves by metallic nanoparticles. Such nanoparticles most often have curvilinear shapes, therefore we propose a numerical modeling strategy which combines the use of an unstructured tetrahedral mesh for the discretization of the scattering structures with a structured (uniform cartesian) mesh for treating efficiently the rest of the domain. The overall goal is to increase the flexibility in the meshing process while decreasing the needs in computational resources for the target applications. The latter are here modeled by the system of 3D time-domain Maxwell equations coupled to a Drude dispersion model for taking into account the material properties of nanoparticles at optical frequencies. We propose an auxiliary differential equation (ADE) based DGTD method for solving the resulting system and present numerical results demonstrating the benefits of using non-conforming multi-element meshes in this particular application context.

1. Introduction

Nanophotonics is a branch of optical engineering which is concerned with the study of the behavior of light at the nanometer scale in interaction with sub-wavelength particles or devices. Because of its numerous scientific and technological applications (e.g. in relation to telecommunication, energy production and biomedicine), nanophotonics currently represents an active field of research increasingly relying on computer simulation besides experimental studies. The numerical study of electromagnetic wave propagation scattered by nanometer scale structures requires taking into account an appropriate physical dispersion model, such as the Drude or Drude–Lorentz models, for characterizing the material properties of the involved nanostructures at optical frequencies [1]. Such a dispersion model allows to establish a dependency between the electrical permittivity and the electrical conductivity of the material and the angular frequency of the incident electromagnetic wave. For so-called *local dispersion models*, one has to deal with the numerical treatment of the system of time-domain Maxwell equations for the electromagnetic field, coupled to a system of auxiliary ordinary differential equations modeling the space–time evolution of the electrical polarization or a polarization current, depending on the considered dispersion models. In these models, one assumes that the response of an electron in the metal only depends on its interaction with the electric field at its precise position. This assumption, called *local response assumption*,

* Corresponding author.
E-mail address: Raphael.Leger@inria.fr (R. Léger).

0377-0427/$ – see front matter
http://dx.doi.org/10.1016/j.cam.2013.12.042

already gives a good description of the underlying physics above the nanometer scale. However, nanofabrication tools are improving a lot, enabling the design of structures approaching subnanometer scales. At this level, new optical properties appear that cannot be accurately described by a local model. In such cases, it becomes necessary to consider a more detailed description of the underlying physics, and alternative physical models of dispersion (see [2] and references therein). These modified models are called *non-local models* [3].

A lot of methods have been developed for the numerical solution of the time-domain Maxwell equations. Finite difference time-domain (FDTD) methods based on Yee's scheme (a time explicit method defined on a staggered mesh) are still prominent because of their simplicity and their non-dissipative nature (they hold an energy conservation property which is an important ingredient in the numerical simulation of unsteady wave propagation problems) [4]. When it comes to the simulation of realistic nanophotonic applications, the FDTD method raises several important limitations, essentially due to the use of a (structured) cartesian discretization grid. In the last ten years, the Discontinuous-Galerkin Time-Domain (DGTD) method has met an increased interest in the purpose of simulating complex industrial problems. Indeed, these methods somehow can be seen as a crossover between Finite Element Time-Domain (FETD) methods (their accuracy depends of the order of a chosen local polynomial basis upon which the solution is represented) and Finite Volume Time-Domain (FVTD) methods (the neighboring cells are connected by numerical fluxes). Thus, DGTD methods offer a wide range of flexibility in terms of geometry (since the use of unstructured and non-conforming meshes is naturally permitted) as well as local approximation order refinement strategies, which are of useful practical interest.

In this study, we focus on the study and development of a parallel non-conforming multi-element DGTD method for the solution of the 3D time-domain Maxwell equations coupled to a Drude dispersion model for metals at frequencies relevant to nanophotonic applications, and in particular for the simulation of the scattering of an electromagnetic by metallic nanoparticles. Such nanoparticles most often have curvilinear shapes, therefore we propose a numerical modeling strategy which combines the use of an unstructured tetrahedral mesh for the discretization of the scattering structures with a structured (uniform cartesian) mesh for treating the rest of the domain. The emphasis of this work is on increasing the flexibility in the meshing process of nanophotonic configurations while decreasing the needs in computational resources for the target applications. In Section 2, after a short description of the modeling issues regarding the considered physical context, we state the initial and boundary value problem at hand. Section 3 is devoted to the formulation of the proposed non-conforming multi-element DGTD method for the solution of the mathematical model introduced in Section 2. Practical implementation and parallelization aspects are discussed in Section 3.5. In Section 4 numerical and performance results are presented for two test problems. First, we consider the scattering of a single nanosphere which allows a comparison with a reference solution in the time-harmonic regime for validation purposes. Then, we apply the proposed parallel numerical methodology to an L-shaped waveguide composed of nanospheres in order to illustrate the benefits of using non-conforming multi-element meshes in this particular application context. Finally, we summarize the outcomes of this study and outline some future works in Section 5.

2. The time-domain Maxwell–Drude equations

To be able to consider concrete physical situations such as the ones characterizing light–matter interactions with nanometer scale objects, one has to take into account in the numerical treatment a better description of the propagation of waves in realistic media. The physical phenomenon that we consider here is dispersion. In the presence of an electric field the medium cannot react instantaneously and thus presents an electric polarization of the molecules or electrons that itself influences the electric displacement. In the case of a linear homogeneous isotropic media, there is a linear relation between the applied electric field and the polarization. However, above some range of frequencies (depending on the considered material), the dispersion phenomenon cannot be neglected and the relation between the polarization and the applied electric field becomes complex. In practice, this is modeled by a frequency dependent complex permittivity. Several such models for the characterization of the permittivity exist; they are established by considering the equation of motion of the electrons in the medium and making some simplifications. If one is interested in taking into account the dispersion effects in metals at the nanometer scale and at optical frequencies, then the Drude model [5] is generally adopted in the first instance. However, for frequency ranges that are too wide, or that include interband transitions of electrons in the metal, it is well-known that the Drude model suffers from severe limitations. In these cases, Drude–Lorentz or even more sophisticated dispersion models are employed [6].

There are mainly two ways of handling the frequency dependent permittivity in the framework of time-domain simulations, both starting from models defined in the frequency domain. The first approach is to introduce the polarization vector as an unknown field through an auxiliary differential equation which is derived from the original model in the frequency domain by means of an inverse Fourier transform. This is called the *Direct Method* or *Auxiliary Differential Equation* (ADE) formulation. One can note that while the new equations can be easily added to any time-domain Maxwell solver, the resulting set of differential equations is tied to the particular choice of dispersive model and will never act as a black box able to deal with other models. In the second approach, the electric field displacement is computed from a time convolution integral of the electric field and the permittivity, of which the formulation can be changed independently from the rest of the solver. This is called the *Recursive Convolution Method* (RCM).

An ADE formulation is adopted here and we focus on the case of a Drude model for the physical dispersion. The Drude model is associated to a particularly simple theory that, for a chosen specific frequency range of interest and a given metallic

material, successfully accounts for the optical and thermal properties of the latter. In this model, the metal is considered as a static lattice of positive ions immersed in a free electrons gas. Those electrons are considered to be the valence electrons of each metallic atom, that got delocalized when put into contact with the potential produced by the rest of the lattice atoms. In the case of the Drude model, the frequency dependent permittivity is given by $\varepsilon_r(\omega) = \varepsilon_\infty - \frac{\omega_d^2}{\omega^2 + i\omega\gamma_d}$ where ε_∞ represents the core electrons contribution to the relative permittivity ε_r, γ_d is a coefficient linked to the electron/ion collisions representing the friction experienced by the electrons and $\omega_d = \sqrt{\frac{n_e e^2}{m_e \varepsilon_0}}$ (m_e is the electron mass, e the electronic charge and n_e the electronic density) is the plasma frequency of the electrons. Considering a constant permeability and a homogeneous and isotropic medium, one can write the Maxwell equations as:

$$\nabla \times \mathbf{H} = \frac{\partial \mathbf{D}}{\partial t}, \qquad \nabla \times \mathbf{E} = -\frac{\partial \mathbf{B}}{\partial t}, \tag{1}$$

along with the constitutive relations $\mathbf{D} = \varepsilon_0 \varepsilon_\infty \mathbf{E} + \mathbf{P}$ and $\mathbf{B} = \mu_0 \mathbf{H}$, which can be combined to yield:

$$\nabla \times \mathbf{E} = -\mu_0 \frac{\partial \mathbf{H}}{\partial t}, \qquad \nabla \times \mathbf{H} = \varepsilon_0 \varepsilon_\infty \frac{\partial \mathbf{E}}{\partial t} + \frac{\partial \mathbf{P}}{\partial t}. \tag{2}$$

In the frequency domain, the polarization $\mathbf{P}$ is linked to the electric field through the relation $\hat{\mathbf{P}} = -\frac{\varepsilon_0 \omega_d^2}{\omega^2 + i\gamma_d \omega} \hat{\mathbf{E}}$, where $\hat{\cdot}$ denotes the Fourier transform of the time-domain field. An inverse Fourier transform gives:

$$\frac{\partial^2 \mathbf{P}}{\partial t^2} + \gamma_d \frac{\partial \mathbf{P}}{\partial t} = \varepsilon_0 \omega_d^2 \mathbf{E}. \tag{3}$$

By defining the dipolar current vector $\mathbf{J}_p = \frac{\partial \mathbf{P}}{\partial t}$, (2)–(3) can be rewritten as:

$$\mu_0 \frac{\partial \mathbf{H}}{\partial t} = -\nabla \times \mathbf{E}, \qquad \varepsilon_0 \varepsilon_\infty \frac{\partial \mathbf{E}}{\partial t} = \nabla \times \mathbf{H} - \mathbf{J}_p, \qquad \frac{\partial \mathbf{J}_p}{\partial t} + \gamma_d \mathbf{J}_p = \varepsilon_0 \omega_d^2 \mathbf{E}. \tag{4}$$

Recalling the definitions of the impedance and light velocity in vacuum, $Z_0 = \sqrt{\mu_0/\varepsilon_0}$ and $c_0 = 1/\sqrt{\varepsilon_0 \mu_0}$, and introducing the following substitutions, $\widetilde{\mathbf{H}} = Z_0 \mathbf{H}$, $\widetilde{\mathbf{E}} = \mathbf{E}$, $\widetilde{\mathbf{J}}_p = Z_0 \mathbf{J}_p$, $\widetilde{t} = c_0 t$, $\widetilde{\gamma}_d = \gamma_d / c_0$ and $\widetilde{\omega}_d^2 = \omega_d^2 / c_0^2$, it can be shown that system (4) can be normalized to yield:

$$\frac{\partial \widetilde{\mathbf{H}}}{\partial t} = -\nabla \times \widetilde{\mathbf{E}}, \qquad \varepsilon_\infty \frac{\partial \widetilde{\mathbf{E}}}{\partial t} = \nabla \times \widetilde{\mathbf{H}} - \widetilde{\mathbf{J}}_p, \qquad \frac{\partial \widetilde{\mathbf{J}}_p}{\partial t} + \gamma_d \widetilde{\mathbf{J}}_p = \widetilde{\omega}_d^2 \widetilde{\mathbf{E}}, \tag{5}$$

knowing that $\mu_0 c_0 / Z_0 = 1$ and $\varepsilon_0 c_0 Z_0 = 1$. From now on, we omit the $\widetilde{X}$ notation for the normalized variables.

Our goal is to solve system (5) in a domain Ω with boundary $\partial\Omega = \Gamma_a \cup \Gamma_m$, where we impose the following boundary conditions: $\mathbf{n} \times \mathbf{E} = 0$ on Γ_m, and $\mathcal{L}(\mathbf{E}, \mathbf{H}) = \mathcal{L}(\mathbf{E}^{\text{inc}}, \mathbf{H}^{\text{inc}})$ on Γ_a where $\mathcal{L}(\mathbf{X}, \mathbf{Y}) = \mathbf{n} \times \mathbf{X} - z\mathbf{n} \times (\mathbf{Y} \times \mathbf{n})$ with $z = \sqrt{\mu/\varepsilon}$. Here $\mathbf{n}$ denotes the unit outward normal to $\partial\Omega$ and $(\mathbf{E}^{\text{inc}}, \mathbf{H}^{\text{inc}})$ is a given incident field. The first boundary condition is called *metallic* (referring to a perfectly electric conducting surface) while the second condition is an *absorbing* boundary condition, more precisely the Silver–Müller condition which is a first order approximation of the exact absorbing boundary condition. This absorbing condition is applied on Γ_a which represents an artificial truncation of the computational domain.

3. DGTD method on multi-element non-conforming meshes

This section is concerned with the numerical treatment of system (5) using a DGTD method. A discontinuous Galerkin formulation can be seen as a classical finite element method for which the global continuity of the approximation has been lifted. This implies that the support of each basis function is restrained to a discretization cell, which leads to local formulations implying no large mass matrix inversion if an explicit time-marching scheme is adopted. Then, connexion between neighboring cells is restored by the use of a numerical flux as in a finite volume method. The form of the numerical flux impacts the mathematical properties of the resulting DGTD scheme. Both centered [7] or upwind [8] fluxes can be used.

The discontinuity of the approximation allows for several methodological improvements such as the local adaptation of the approximation order [9], and the use of non-conforming meshes [10,11]. Besides, the method is particularly well suited to an implementation on modern high performance computing platforms [12]. Also, a wide choice of time integration schemes can be used for the discretization of time derivatives, including the leap-frog and Runge–Kutta schemes. Moreover, local time-stepping [13] as well as locally implicit formulations [14] have been extensively studied during the last years in the discontinuous Galerkin framework. DGTD methods have now acquired a sufficient level of maturity and have successfully penetrated several scientific and technological communities following their adaptation to increasingly complex modeling contexts such as [15–18] among others. Worthwhile to note, the method has also been adopted for the first time in a commercial software as the time-domain alternative of a very well known electromagnetic wave simulation tool [19]. In all the previously mentioned works on DGTD methods, the first order (or mixed) form of the system of time-domain Maxwell equations is considered and, within each mesh element, the electromagnetic field components are approximated by an arbitrarily high order nodal polynomial.

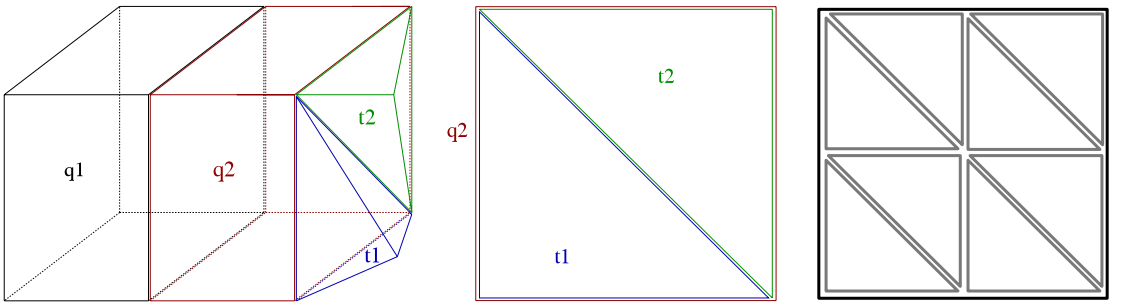

Fig. 1. Left: type of non-conformity considered in 3D (here, $l = 1$), between a hexahedron (q2) and two tetrahedra (t1 and t2). Middle: 2D view of the non-conforming hybrid face between q2 and, t1 and t2. Right: other example (2D view only) of non-conformity considered, between one hexahedron and eight tetrahedra ($l = 2$).

3.1. Discretization in space

We consider a discretization of the domain Ω as $\mathscr{C}_h = \bigcup_{i=1}^{N} c_i = \mathscr{T}_h \bigcup \mathscr{Q}_h$ where the c_i's are hexahedral ($\in \mathscr{Q}_h$) and tetrahedral ($\in \mathscr{T}_h$) elements. Moreover, we impose that the hexahedral mesh is orthogonal i.e. that it is a cartesian mesh. The resulting mesh is hybrid and non-conforming (i.e. with hanging nodes on a common face between two elements with different types) [11,9,10]. In this study, we assume a certain kind of non-conformity as shown in Fig. 1, i.e. we limit ourselves to configurations such that for a given non-conforming interface, the triangular faces on one side are obtained by subdividing the quadrangular face on the other side. In practice, we allow for an arbitrary refinement level l of the triangular faces ($l = 1$ and $l = 2$ on Fig. 1).

3.2. Definitions and notations

We introduce $\mathbb{P}_p[c_i]$ the space of scalar polynomial functions with degree at most p in $c_i \in \mathscr{T}_h$, and $\mathbb{Q}_r[c_i]$ the space of scalar polynomial functions with degree at most r with respect to each space variable separately in $c_i \in \mathscr{Q}_h$. Depending on the case, d_i stands for the dimension of $\mathbb{P}_p[c_i]$ or $\mathbb{Q}_r[c_i]$. We seek for the discrete approximations $\mathbf{E}_h$, $\mathbf{H}_h$ and $\mathbf{J}_{p,h}$ of $\mathbf{E}$, $\mathbf{H}$ and $\mathbf{J}_p$, each of them being searched for in the approximation space V_h^3 defined by:

$$V_h = \left\{ v_h \in L^2(\Omega) \,\middle|\, \begin{matrix} \forall c_i \in \mathscr{T}_h, \;\; v_h|_{c_i} \in \mathbb{P}_p[c_i] \\ \forall c_i \in \mathscr{Q}_h, \;\; v_h|_{c_i} \in \mathbb{Q}_r[c_i] \end{matrix} \right\}. \tag{6}$$

The resulting DGTD method will be denoted as DGTD-$\mathbb{P}_p\mathbb{Q}_r$ in the sequel. Let $a_{ik} = c_i \cap c_k$ be a common interface between c_i and c_k and let us denote by $\mathcal{V}_i = \{k | c_i \cap c_k \neq \varnothing\}$ the set of neighboring cells of c_i. We also introduce $\check{\mathbf{n}}_{ik}$ which is the unitary normal vector on a_{ik} directed from c_i to c_k, and $\check{\mathbf{n}}_{ik} = (\check{n}_{ik}^1, \check{n}_{ik}^2, \check{n}_{ik}^3)^{\mathrm{T}} \in \mathbb{R}^3$. We also have an equivalent notation $\check{\mathbf{n}}_i$ for the outward unitary normal to the cell boundary ∂c_i.

3.2.1. Weak formulation

It is now possible to write the weak formulation of the problem (5). By taking the dot-product of each term with a *vectorial* test function $\boldsymbol{\psi}$ and then integrating over cell c_i, one obtains the following variational problem:

$$\begin{cases} \displaystyle\int_{c_i} \frac{\partial \mathbf{H}}{\partial t} \cdot \boldsymbol{\psi} + \int_{c_i} \nabla \times \mathbf{E} \cdot \boldsymbol{\psi} = 0, \\ \displaystyle\int_{c_i} \varepsilon_\infty \frac{\partial \mathbf{E}}{\partial t} \cdot \boldsymbol{\psi} - \int_{c_i} \nabla \times \mathbf{H} \cdot \boldsymbol{\psi} = - \int_{c_i} \mathbf{J}_p \cdot \boldsymbol{\psi}, \\ \displaystyle\int_{c_i} \frac{\partial \mathbf{J}_p}{\partial t} \cdot \boldsymbol{\psi} + \int_{c_i} \gamma_d \mathbf{J}_p \cdot \boldsymbol{\psi} = \int_{c_i} \omega_d^2 \mathbf{E} \cdot \boldsymbol{\psi}. \end{cases} \tag{7}$$

Using the classical Green formulae, this writes:

$$\begin{cases} \displaystyle\int_{c_i} \frac{\partial \mathbf{H}}{\partial t} \cdot \boldsymbol{\psi} + \int_{c_i} \mathbf{E} \cdot \nabla \times \boldsymbol{\psi} = \int_{\partial c_i} \left(\mathbf{E} \times \check{\mathbf{n}}_i\right) \cdot \boldsymbol{\psi}, \\ \displaystyle\int_{c_i} \varepsilon_\infty \frac{\partial \mathbf{E}}{\partial t} \cdot \boldsymbol{\psi} - \int_{c_i} \mathbf{H} \cdot \nabla \times \boldsymbol{\psi} = - \int_{c_i} \mathbf{J}_p \cdot \boldsymbol{\psi} - \int_{\partial c_i} \left(\mathbf{H} \times \check{\mathbf{n}}_i\right) \cdot \boldsymbol{\psi}, \\ \displaystyle\int_{c_i} \frac{\partial \mathbf{J}_p}{\partial t} \cdot \boldsymbol{\psi} + \int_{c_i} \gamma_d \mathbf{J}_p \cdot \boldsymbol{\psi} = \int_{c_i} \omega_d^2 \mathbf{E} \cdot \boldsymbol{\psi}. \end{cases}$$

We now define a set of scalar basis functions ϕ_{ij} ($1 \leq j \leq d_i$) on the cell c_i. Since the test functions are to be naturally chosen as vectorial elements, one should define three vectorial basis functions (for the three space dimensions) for each scalar one. We therefore introduce:

$$\boldsymbol{\phi}_{ij}^1 = \begin{bmatrix} \phi_{ij} \\ 0 \\ 0 \end{bmatrix}, \qquad \boldsymbol{\phi}_{ij}^2 = \begin{bmatrix} 0 \\ \phi_{ij} \\ 0 \end{bmatrix} \quad \text{and} \quad \boldsymbol{\phi}_{ij}^3 = \begin{bmatrix} 0 \\ 0 \\ \phi_{ij} \end{bmatrix}.$$

We denote by $\mathbf{E}_i$ the restriction of $\mathbf{E}_h$ to the cell c_i, i.e. $\mathbf{E}_i = \mathbf{E}_h|_{c_i}$, where $\mathbf{E}_i$ is locally expanded as:

$$\mathbf{E}_i = \sum_{m=1}^{3} \sum_{j=1}^{d_i} E_{ij}^m \boldsymbol{\phi}_{ij}^m,$$

with similar expressions for $\mathbf{H}_i$ and $\mathbf{J}_{p,i}$. We now choose the test functions $\boldsymbol{\psi}$ to be the $3\,d_i$ vectors $\boldsymbol{\phi}_{ij}^m$ for $1 \leq m \leq 3$ and $1 \leq j \leq d_i$. Then, since the approximate fields $\mathbf{E}_h$ and $\mathbf{H}_h$ are allowed to be discontinuous across element boundaries, a specific treatment must be introduced when evaluating such a field at a cell boundary. In the context of finite volume methods, this leads to the notion of *numerical flux*. In the present study, we choose to use a centered approximation to evaluate $\mathbf{E}_h|_{a_{ik}}$, i.e. $\forall i, \forall k \in \mathcal{V}_i$ we set $\mathbf{E}_h|_{a_{ik}} = (\mathbf{E}_i|_{a_{ik}} + \mathbf{E}_j|_{a_{ik}})/2$ (a similar treatment is applied to $\mathbf{H}_h$). Taking into account the previous definitions, one obtains the following $9\,d_i$ scalar equations:

$$\begin{cases} \displaystyle\int_{c_i} \frac{\partial \mathbf{H}_i}{\partial t} \cdot \boldsymbol{\phi}_{ij}^m + \int_{c_i} \mathbf{E}_i \cdot \nabla \times \boldsymbol{\phi}_{ij}^m = \sum_{k \in \mathcal{V}_i} \int_{a_{ik}} \left(\boldsymbol{\phi}_{ij}^m \times \frac{\mathbf{E}_i + \mathbf{E}_k}{2} \right) \cdot \breve{\mathbf{n}}_{ik}, \\ \displaystyle\int_{c_i} \varepsilon_\infty \frac{\partial \mathbf{E}_i}{\partial t} \cdot \boldsymbol{\phi}_{ij}^m - \int_{c_i} \mathbf{H}_i \cdot \nabla \times \boldsymbol{\phi}_{ij}^m = -\int_{c_i} \mathbf{J}_{p,i} \cdot \boldsymbol{\phi}_{ij}^m - \sum_{k \in \mathcal{V}_i} \int_{a_{ik}} \left(\boldsymbol{\phi}_{ij}^m \times \frac{\mathbf{H}_i + \mathbf{H}_k}{2} \right) \cdot \breve{\mathbf{n}}_{ik}, \\ \displaystyle\int_{c_i} \frac{\partial \mathbf{J}_{p,i}}{\partial t} \cdot \boldsymbol{\phi}_{ij}^m + \int_{c_i} \gamma_d \mathbf{J}_{p,i} \cdot \boldsymbol{\phi}_{ij}^m = \int_{c_i} \omega_d^2 \mathbf{E}_i \cdot \boldsymbol{\phi}_{ij}^m. \end{cases}$$

Performing an integration by parts on the surface integrals leads to:

$$\begin{cases} \displaystyle\int_{c_i} \frac{\partial \mathbf{H}_i}{\partial t} \cdot \boldsymbol{\phi}_{ij}^m = -\frac{1}{2} \int_{c_i} \left(\mathbf{E}_i \cdot \nabla \times \boldsymbol{\phi}_{ij}^m + \nabla \times \mathbf{E}_i \cdot \boldsymbol{\phi}_{ij}^m \right) + \frac{1}{2} \sum_{k \in \mathcal{V}_i} \int_{a_{ik}} \boldsymbol{\phi}_{ij}^m \cdot \left(\mathbf{E}_k \times \breve{\mathbf{n}}_{ik} \right), \\ \displaystyle\int_{c_i} \varepsilon_\infty \frac{\partial \mathbf{E}_i}{\partial t} \cdot \boldsymbol{\phi}_{ij}^m = \frac{1}{2} \int_{c_i} \left(\mathbf{H}_i \cdot \nabla \times \boldsymbol{\phi}_{ij}^m + \nabla \times \mathbf{H}_i \cdot \boldsymbol{\phi}_{ij}^m \right) - \int_{c_i} \mathbf{J}_{p,i} \cdot \boldsymbol{\phi}_{ij}^m - \frac{1}{2} \sum_{k \in \mathcal{V}_i} \int_{a_{ik}} \boldsymbol{\phi}_{ij}^m \cdot \left(\mathbf{H}_k \times \breve{\mathbf{n}}_{ik} \right) \\ \displaystyle\int_{c_i} \frac{\partial \mathbf{J}_{p,i}}{\partial t} \cdot \boldsymbol{\phi}_{ij}^m + \int_{c_i} \gamma_d \mathbf{J}_{p,i} \cdot \boldsymbol{\phi}_{ij}^m = \int_{c_i} \omega_d^2 \mathbf{E}_i \cdot \boldsymbol{\phi}_{ij}^m. \end{cases} \tag{8}$$

3.2.2. Semi-discrete equations

The previous equations can be cast under a matrix form using the decomposition of each fields on the basis. Terms of the type $\displaystyle\int_{c_i} \varepsilon_\infty \frac{\partial \mathbf{E}_i}{\partial t} \cdot \boldsymbol{\phi}_{ij}^m$ can be written as $\mathbb{M}_i^{\varepsilon_\infty} \frac{\partial \overline{\mathbf{E}}_i}{\partial t}$ with $\mathbb{M}_i^{\varepsilon_\infty} = \begin{bmatrix} \widetilde{\mathbb{M}}_i^{\varepsilon_\infty} & \mathbf{0}_{d_i \times d_i} & \mathbf{0}_{d_i \times d_i} \\ \mathbf{0}_{d_i \times d_i} & \widetilde{\mathbb{M}}_i^{\varepsilon_\infty} & \mathbf{0}_{d_i \times d_i} \\ \mathbf{0}_{d_i \times d_i} & \mathbf{0}_{d_i \times d_i} & \widetilde{\mathbb{M}}_i^{\varepsilon_\infty} \end{bmatrix}$ defined by its diagonal blocks $\left(\widetilde{\mathbb{M}}_i^{\varepsilon_\infty}\right)_{jl} = \displaystyle\int_{c_i} \varepsilon_\infty \phi_{ij} \phi_{il}$ and $\overline{\mathbf{E}}_i = \begin{bmatrix} (E_{x,ij})_{1 \leqslant j \leqslant d_i} \\ (E_{y,ij})_{1 \leqslant j \leqslant d_i} \\ (E_{z,ij})_{1 \leqslant j \leqslant d_i} \end{bmatrix}$ that has $3\,d_i$ components. Reasoning similarly for the other terms allows to rewrite (8) as:

$$\begin{cases} \mathbb{M}_i \dfrac{\partial \overline{\mathbf{H}}_i}{\partial t} = -\mathbb{K}_i \overline{\mathbf{E}}_i + \displaystyle\sum_{k \in \mathcal{V}_i} \mathbb{S}_{ik} \overline{\mathbf{E}}_k, \\ \mathbb{M}_i^{\varepsilon_\infty} \dfrac{\partial \overline{\mathbf{E}}_i}{\partial t} = \mathbb{K}_i \overline{\mathbf{H}}_i - \displaystyle\sum_{k \in \mathcal{V}_i} \mathbb{S}_{ik} \overline{\mathbf{H}}_k - \mathbb{M}_i \bar{\mathbf{J}}_{p,i}, \\ \dfrac{\partial \bar{\mathbf{J}}_{p,i}}{\partial t} + \gamma_d \mathbf{J}_{p,i} = \omega_d^2 \mathbf{E}_i, \end{cases}$$

where the $3\,d_i \times 3\,d_i$ local stiffness matrix $\mathbb{K}_i$ and the $3\,d_i \times 3\,d_k$ surface matrix $\mathbb{S}_{ik}$ are defined by their respective diagonal blocks:

$$\begin{aligned} \left(\widetilde{\mathbb{K}}_i\right)_{jl} &= \frac{1}{2} \int_{c_i} \left(\boldsymbol{\phi}_{ij}^m \cdot \nabla \times \boldsymbol{\phi}_{il}^m + \boldsymbol{\phi}_{il}^m \cdot \nabla \times \boldsymbol{\phi}_{ij}^m \right), \text{ of size } d_i \times d_i, \\ \left(\widetilde{\mathbb{S}}_{ik}\right)_{jl} &= \frac{1}{2} \int_{a_{ik}} \boldsymbol{\phi}_{ij}^m \cdot \left(\boldsymbol{\phi}_{kl}^m \times \breve{\mathbf{n}}_{ik} \right), \text{ of size } d_i \times d_k. \end{aligned} \tag{9}$$

Different possibilities exist for the choice of the basis functions ϕ_{ij}. A common choice consists in using Lagrange polynomials, though other choices are possible. A set of $p_i + 1$ interpolation nodes $(x_j)_{0\leqslant j\leqslant p_i}$ is defined in the cell, and the basis functions are then the Lagrange function $L_k^p(x)$ equal to 1 on the x_k node, and to 0 on all the other $x_j, j \neq k$.

Particular comments apply to the computation of the coefficients of the interface matrix $\widetilde{\mathbb{S}}_{ik}$. Indeed, depending on the type of face, we shall make the following distinctions:

- Conforming internal interface. To calculate the coefficients of the interface matrix $\widetilde{\mathbb{S}}_{ik}$ for a conforming interface a_{ik} between two tetrahedra (two hexahedra, respectively), we use a precomputed matrix on a reference triangular (quadrangular, respectively) element and an affine mapping to deduce the matrices on physical interfaces. This precalculated matrix does not depend on the underlying mesh but it requires that the conformity is ensured between any two adjacent elements.
- Non-conforming (hybrid) internal interface. As mentioned in Section 3.1, in 3D, the intersection between two neighboring tetrahedral and hexahedral elements necessarily presents hanging nodes. Therefore, one has to compute the interface matrix corresponding to such a hybrid and non-conforming interface using an appropriate numerical integration procedure. Given the type of non-conformity that we allow in the meshing process (see Section 3.1), all the hybrid interfaces are triangles. On these triangles, we use the Gauss–Legendre quadrature formulae that are fully described in [20]. The method to calculate the matrix associated with an interface between a tetrahedron c_i and a hexahedron c_k goes as follows. First, note that the surface matrix $\widetilde{\mathbb{S}}_{ik}$ (cf. (9)) involves terms of the normal $\breve{\mathbf{n}}_{ik}$ as well as a $(d_i \times d_k)$ matrix $\widetilde{\Phi}_{ik}$ defined by: $(\widetilde{\Phi}_{ik})_{jl} = \int_{a_{ik}} \phi_{ij}\phi_{kl}$, for $1 \leq j \leq d_i$, $1 \leq l \leq d_k$. Second, we call N_{GL} the minimal number of Gauss points and weights necessary to obtain an exact integration of polynomials of degree $\leq 2N_{GL} - 1$. The actual computation of the matrix Φ_{ik} is of the form:

  $$\widetilde{\Phi}_{ik} \simeq P^1 B \left(P^2\right)^{\mathrm{T}},$$

  with:

  $$\begin{cases} (\widetilde{P}^1)_{jl} = \phi_{ij}(\mathbf{x}^l), & \text{for } 1 \leq j \leq d_i \text{ and } 1 \leq l \leq N_{GL}, \\ (\widetilde{P}^2)_{jl} = \phi_{kj}(\mathbf{x}^l), & \text{for } 1 \leq j \leq d_k \text{ and } 1 \leq l \leq N_{GL}, \\ (\widetilde{B})_{ll} = \omega_l \quad \text{and} \quad (\widetilde{B})_{jl} = 0 & \text{if } j \neq l, \text{ for } 1 \leq j, l \leq N_{GL}, \end{cases}$$

  where $\mathbf{x}^l$ and ω_l are respectively the points and weights of Gauss–Legendre method. The matrices P^1 and P^2 are respectively of size of $d_i \times N_{GL}$ and $d_k \times N_{GL}$, the matrix B is diagonal and of dimension $N_{GL} \times N_{GL}$.
- Boundary interface. For the boundary cells i.e. for interfaces located on the discretization of Γ, we consider that c_k is a fictitious cell and $\mathbf{W}_k$ is defined according to the boundary conditions that are set on Γ. For instance, if $a_{ik} \in \Gamma_m$ we set:

  $$\begin{pmatrix} \mathbf{E}_k \\ \mathbf{H}_k \end{pmatrix} = \begin{bmatrix} -I_{3\times3} & \mathbf{0}_{3\times3} \\ \mathbf{0}_{3\times3} & I_{3\times3} \end{bmatrix} \begin{pmatrix} \mathbf{E}_i \\ \mathbf{H}_i \end{pmatrix}, \quad \text{i.e.} \quad \begin{pmatrix} \mathbf{E}_k \\ \mathbf{H}_k \end{pmatrix} = \begin{pmatrix} -\mathbf{E}_i \\ \mathbf{H}_i \end{pmatrix}.$$

  If $a_{ik} \in \partial\Gamma_a$ we set:

  $$\begin{pmatrix} \mathbf{E}_k \\ \mathbf{H}_k \end{pmatrix} = \begin{bmatrix} \mathbf{0}_{3\times3} & Z_i N_{ik} \\ -Z_i^{-1} N_{ik} & \mathbf{0}_{3\times3} \end{bmatrix} \begin{pmatrix} \mathbf{E}_i \\ \mathbf{H}_i \end{pmatrix} + \begin{bmatrix} I_{3\times3} & -Z_i N_{ik} \\ Z_i^{-1} N_{ik} & I_{3\times3} \end{bmatrix} \begin{pmatrix} \mathbf{E}_i^{\mathrm{inc}} \\ \mathbf{H}_i^{\mathrm{inc}} \end{pmatrix},$$

  where $N_{ik} = \begin{bmatrix} 0 & \breve{n}_{ik}^3 & -\breve{n}_{ik}^2 \\ -\breve{n}_{ik}^3 & 0 & \breve{n}_{ik}^1 \\ \breve{n}_{ik}^2 & -\breve{n}_{ik}^1 & 0 \end{bmatrix}$ and $\begin{pmatrix} \mathbf{E}_i^{\mathrm{inc}} \\ \mathbf{H}_i^{\mathrm{inc}} \end{pmatrix}$ is a given incident field.

3.3. Time integration

A second-order leap-frog scheme (LF2) is used for time integration. In doing so $\overline{\mathbf{E}}_i$ is evaluated at time station $t^n = n\Delta t$, whereas $\overline{\mathbf{H}}_i$, $\bar{\mathbf{J}}_{p,i}$ are evaluated at time station $t^{n+\frac{1}{2}} = \left(n + \frac{1}{2}\right)\Delta t$. This leads to seek the values of $\overline{\mathbf{E}}_i^{n+1}$, $\overline{\mathbf{H}}_i^{n+\frac{3}{2}}$ and $\bar{\mathbf{J}}_{p,i}^{n+\frac{3}{2}}$ knowing those of $\overline{\mathbf{E}}_i^{n}$, $\overline{\mathbf{H}}_i^{n+\frac{1}{2}}$ and $\bar{\mathbf{J}}_{p,i}^{n+\frac{1}{2}}$ with the following discretization:

$$\begin{cases} \dfrac{\mathbb{M}_i^{\varepsilon\infty}}{\Delta t}\left(\overline{\mathbf{E}}_i^{n+1} - \overline{\mathbf{E}}_i^{n}\right) = \mathbb{K}_i \overline{\mathbf{H}}_i^{n+\frac{1}{2}} - \displaystyle\sum_{k\in\mathcal{V}_i} \mathbb{S}_{ik} \overline{\mathbf{H}}_k^{n+\frac{1}{2}} - \mathbb{M}_i \bar{\mathbf{J}}_{p,i}^{n+\frac{1}{2}}, \\ \dfrac{\mathbb{M}_i}{\Delta t}\left(\overline{\mathbf{H}}_i^{n+\frac{3}{2}} - \overline{\mathbf{H}}_i^{n+\frac{1}{2}}\right) = -\mathbb{K}_i \overline{\mathbf{E}}_i^{n+1} + \displaystyle\sum_{k\in\mathcal{V}_i} \mathbb{S}_{ik} \overline{\mathbf{E}}_k^{n+1}, \\ \dfrac{1}{\Delta t}\left(\bar{\mathbf{J}}_{p,i}^{n+\frac{3}{2}} - \bar{\mathbf{J}}_{p,i}^{n+\frac{1}{2}}\right) = \omega_d^2 \overline{\mathbf{E}}_i^{n+1} - \dfrac{\gamma_d}{2}\left(\bar{\mathbf{J}}_{p,i}^{n+\frac{3}{2}} + \bar{\mathbf{J}}_{p,i}^{n+\frac{1}{2}}\right). \end{cases} \tag{10}$$

Note that different time discretization can be used, like a fourth-order leap frog (LF4) scheme or fourth-order Runge–Kutta (RK4) scheme, under their respective stability conditions.

3.4. Theoretical aspects

We shall now briefly discuss some theoretical aspects concerning the previously introduced DGTD scheme, namely stability and convergence. Compared to the standard analysis developed for pure Maxwell's equations (i.e. for a non-dispersive medium) and a conforming tetrahedral mesh [7], two difficulties arise. The first one is related to the dispersive nature of the media, leading to the coupling of Maxwell's equations with an ordinary differential equation describing the evolution of the polarization current. The corresponding numerical analysis for a DGTD method formulated on a conforming tetrahedral mesh can be found in [21]. The second difficulty relies on the hybrid nature of the mesh. For pure Maxwell's equations (i.e. non-dispersive) but hybrid meshes, the convergence analysis can be found in [22]. The results stated below only rely on the combination of arguments of the two above-cited references. Thus, for clarity and in order to be as concise as possible, we will only state the final results and point out some key points of the proofs.

The total fully discrete energy of the system is defined as $\xi^n = \sum_i \xi_i^n$, where

$$\xi_i^n = \frac{1}{2}\left(\int_{c_i} \mathbf{H}_i^{n+\frac{1}{2}} \cdot \mathbf{H}_i^{n-\frac{1}{2}} + \varepsilon_\infty \int_{c_i} \|\mathbf{E}_i^n\|^2 + \frac{1}{\omega_d^2}\int_{c_i} \mathbf{J}_i^{n+\frac{1}{2}} \cdot \mathbf{J}_i^{n-\frac{1}{2}}\right). \tag{11}$$

Proposition 3.1. *Under a CFL condition of the type $\Delta t \leq Ch$, the fully discrete energy ξ^n is positive and bounded. The scheme is thus stable.*

Sketch of the proof: The proof relies on inverse inequalities and arguments that are standard in numerical analysis. In the first step, one proves that the energy is a positive definite form under a CFL-like condition. There are two key points that differ from a standard analysis here. On the one hand, the energy is split into a part relating tetrahedra cells and another one relating hexahedra cells. Then one treats each of them separately. The added terms containing the hybrid parts have to be treated carefully, but do not add any theoretical difficulty to the proof. On the other hand, in comparison to a pure Maxwell problem, the polarization current energy term can also be negative. Using the ODE describing the evolution of the polarization allows to conclude with standard arguments. The second step is to obtain a bound on the energy. Writing a discrete energy principle using the equation describing the evolution of the field, the analysis here is quite standard and follows [21,22]. Let us notice that due to the polarization current here, the fully discrete energy is not decreasing but remains bounded.

Then we can also state an a priori convergence result.

Theorem 3.2 (*Convergence of the Fully-Discrete Scheme*)**.** *Let $\left(\mathbf{H}, \mathbf{E}, \mathbf{J}_p\right)$ be the solution of (7) and $\left(\mathbf{H}_h^{n+\frac{1}{2}}, \mathbf{E}_h^n, \mathbf{J}_{p,h}^{n+\frac{1}{2}}\right) \in V_h^9$ the fully-discrete solution of (10). If $\left(\mathbf{H}, \mathbf{E}, \mathbf{J}_p\right) \in \mathcal{C}^0([0,T], H^{s+1}(\Omega)^9) \cap \mathcal{C}^3([0,T], L^2(\Omega)^9)$ for $s \geq 0$, then:*

$$\max_n \left(\|\mathbf{H}(t^{n+\frac{1}{2}}) - \mathbf{H}_h^{n+\frac{1}{2}}\|^2 + \|\mathbf{E}(t^n) - \mathbf{E}_h^n\|^2 + \|\mathbf{J}_p(t^{n+\frac{1}{2}}) - \mathbf{J}_{p,h}^{n+\frac{1}{2}}\|^2\right)^{\frac{1}{2}} = O(\Delta t^2 + h^{\min(s,p,r)}).$$

Sketch of the Proof. We also refer to [22,21] for details on the techniques used. Firstly, one proves the convergence of the semi-discrete scheme as defined in (8). The proof relies on the use of an L^2-interpolator (and the associated interpolation error estimates) and inverse inequalities. The sub-optimal h-convergence rate obtained is due to the choice of a centered fluxes formulation. Secondly, the error between the semi-discrete fields and the fully discrete ones is estimated (in the L^2-norm). To this end, one first studies the consistency error (in the ODE sense) and then, by similar energy techniques as for the stability analysis, one is able to prove the convergence.

3.5. Practical implementation and adaptation to parallel platforms

As mentioned previously, the basis functions ϕ_{ij} are nodal, Lagrange polynomials. In our implementation of the proposed DGTD-$\mathbb{P}_p\mathbb{Q}_r$ method, up to 4th order polynomials have been considered on both tetrahedra ($\mathbb{P}_4$) and hexahedra ($\mathbb{Q}_4$), which respectively represents 35 and 125 evenly distributed degrees of freedom per element. It is interesting to remark that, conveniently, only the degrees of freedom geometrically belonging to an interface a_{ik} couple the two elements sharing that interface, which is an intrinsic property of Lagrange basis functions (for both tetrahedra and hexahedra). In other words, the entries of the interface matrices $\widetilde{\mathbb{S}}_{ik}$ (or $\mathbb{S}_{ik}$ equivalently) involving a degree of freedom that does not belong to the interface are equal to zero. This property can be taken into account in order to avoid unnecessary multiplications by 0 when evaluating the elementary numerical fluxes on a_{ik}, thus saving CPU resources. For simplicity, let us define $\mathbf{A}_{\mathbf{H},i}$ (respectively $\mathbf{A}_{\mathbf{E},i}$) as the right hand side of the first (respectively the second) equation of system (10). The time advancing procedure itself consists, first, in advancing $\mathbf{E}_h$, to time $(n+1)\Delta t$ which is based on the following 3 steps sequence—where $\overline{\mathbf{H}}_k$ and $\bar{\mathbf{J}}_{p,i}$ are given at time $(n+1/2)\Delta t$:

Table 1
Characteristics of the tetrahedral and hybrid hexahedral–tetrahedral meshes used for the simulation of the scattering of a plane wave by a single nanosphere.

Method	# vertices	# tetra	# hexa	# d.o.f	Volume
DGTD-$\mathbb{P}_2$	148,618	881,154	0	8,811,540	4.2×10^{-21} m^3
DGTD-$\mathbb{P}_2\mathbb{Q}_2$	93,346	342,499	32,256	4,295,902	8.0×10^{-21} m^3

1. Loop over the conforming interfaces a_{ik} – triangles and quadrangles – of the mesh, and apply the square matrix $\mathbb{S}_{ik}$ (respectively $\mathbb{S}_{ki}$) to the unknown field $\overline{\mathbf{H}}_k$ (respectively $\overline{\mathbf{H}}_i$). Add this contribution to the global flux $\mathbf{A}_{\mathbf{E},i}$ (respectively add it to $\mathbf{A}_{\mathbf{E},k}$).
2. Loop over the non-conforming interfaces a_{ik} – triangles – of the mesh, and apply the rectangular $3d_i \times 3d_k$ matrix $\mathbb{S}_{ik}$ (respectively $3d_k \times 3d_i$ matrix $\mathbb{S}_{ki}$) to the unknown field $\overline{\mathbf{H}}_k$ (respectively $\overline{\mathbf{H}}_i$). Add this contribution to the global flux $\mathbf{A}_{\mathbf{E},i}$ (respectively add it to $\mathbf{A}_{\mathbf{E},k}$).
3. Loop over the cells c_i and apply $\mathbb{K}_i$ to the unknown field $\overline{\mathbf{H}}_i$. Add this contribution to $\mathbf{A}_{\mathbf{E},i}$. Then, during the same run, after the computation of the stiffness step is complete, apply the inverse of the mass matrix $\mathbb{M}_i^{\varepsilon_\infty}$. Finally, if c_i lies in a dispersive material, add the contribution of the current, $\overline{\mathbf{J}}_{p,i}$, to $\mathbf{A}_{\mathbf{E},i}$.

Then, $\mathbf{H}_h$ is advanced to time $(n+3/2)\Delta t$ in a symmetrical manner (except that no current is involved). Finally, the current $\mathbf{J}_{p,h}$ is advanced to time $(n+3/2)\Delta t$. For this, note that as the formulation is local, no matrix–vector product is involved.

Besides, the implementation of the proposed DGTD-$\mathbb{P}_p\mathbb{Q}_r$ method has been adapted to distributed memory parallel computing platforms by adopting a coarse grain parallelization strategy combining a partitioning of the mesh into K submeshes using the MeTiS [23] library and a message passing programming with the MPI standard. In this strategy, each of the K submeshes is treated by a single computing unit (core). A particular concern for this kind of heterogeneous space-discretization method is found in obtaining a partitioning that is sufficiently well-balanced in terms of computational load per subdomain in order to observe a satisfying scalability. However, it is possible to assign heterogeneous weights to the cells of the mesh that MeTiS will use to distribute the computational load as evenly as possible between the subdomains. A straightforward choice having given convincing results so far for the DGTD-$\mathbb{P}_p\mathbb{Q}_r$ method is to define these weights as the number of DOF for each cell. Once the K-way partitioning is achieved, it is necessary to build communication lists including the corresponding artificial faces of each subdomain. For this preprocessing step, the non-conforming interfaces need to be taken into account cautiously. In fact, a non-conforming quadrangular artificial face of a given subdomain may correspond to several non-conforming triangular faces, possibly belonging to different submeshes. Consequently, these quadrangular faces may appear more than once throughout the communication lists.

4. Numerical and performance results

4.1. Near-field resonance of an Au-nanosphere

In order to validate the method and conduct a preliminary assessment of its computational efficiency, we first consider an academic problem which consists in simulating the near-field, sub-wavelength resonance of a single 20 nm radius gold nanosphere lying in vacuum under a plane wave excitation. For this test problem, it is possible to compare the computed numerical solutions to an analytical one in the frequency domain, given by the Mie theory [24], which predicts a surface plasmon resonance, *e.g.* a collective coherent oscillation of the electronic gas described by the Drude model. The source is set as an incident plane wave polarized on the x component, incoming from the artificial domain boundary Γ_a and propagating along the z axis. The incident field is given by $E_x^{\text{inc}}(t) = \sin(2\pi f_c(t-4\tau))\ \mathrm{e}^{-\left(\frac{t-4\tau}{\tau}\right)^2}$. We set $f_c = 576.92$ THz and $\tau = 2.0$ fs. The physical parameters for the sphere are set to $\varepsilon_\infty = 1$, $\omega_d = 1.19 \times 10^4$ THz and $\gamma_d = 141$ THz. We note that in vacuum, the wavelength is approximately 520 nm which is very large compared to the scattering structure. However, the mesh has to be fine enough in order to correctly approximate the obstacle geometry, which has an important impact on both the resonance pattern and amplitude. In fact, for this kind of problem, the most relevant criterion for an a priori assessment of the accuracy of the simulation essentially resides in the geometrical approximation of the scatterer rather than in the number of degrees of freedom per wavelength. This test problem has been simulated using a DGTD-$\mathbb{P}_2$ method applied on a fully tetrahedral mesh and a DGTD-$\mathbb{P}_2\mathbb{Q}_2$ method applied on a non-conforming hexahedral–tetrahedral mesh. The two meshes are partially visualized on Fig. 2 and their characteristics are summarized in Table 1. The computational domain is artificially bounded by a 200 nm diameter sphere in the case of the fully tetrahedral mesh, and by a cube with 200 nm side length in the case of the non-conforming hexahedral–tetrahedral mesh. In both cases we compute the solution until the final physical time $t_f = 20$ fs. The time steps for the DGTD-$\mathbb{P}_2$ and DGTD-$\mathbb{P}_2\mathbb{Q}_2$ methods are $\Delta t_{\text{tet}} = 13.7 \times 10^{-5}$ fs and $\Delta t_{\text{hyb}} = 13.5 \times 10^{-5}$ fs respectively.

On Fig. 3 we plot the distribution of the modulus of the discrete Fourier transform at the source central frequency f_c of the electric field in the plane $z = 0$. We observe a very good agreement between the Mie solution and the two DGTD solutions.

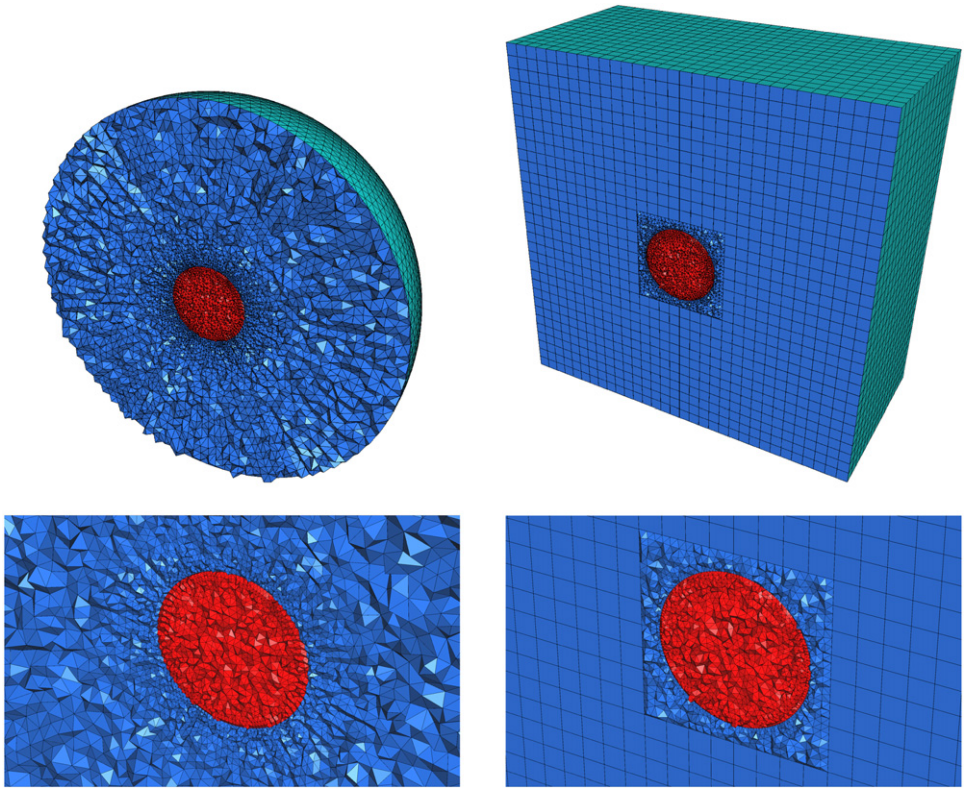

Fig. 2. Partial views of the tetrahedral and hybrid hexahedral–tetrahedral meshes used for the simulation of the scattering of a plane wave by a single nanosphere.

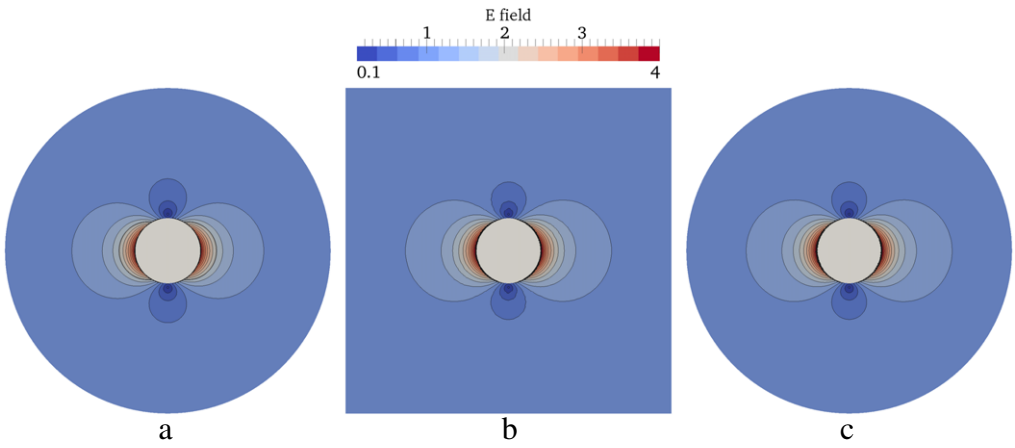

Fig. 3. Simulation of the scattering of a plane wave by a single nanosphere. Module of the electric field in the Fourier domain: (a) Mie analytical solution / (b) DGTD-$\mathbb{P}_2\mathbb{Q}_2$ result / (c) DGTD-$\mathbb{P}_2$ result (the Au-sphere is hidden).

This is also observed on Fig. 4 which represents a 1D cut along the x axis, as well as, in particular, the difference between the numerical DGTD solutions and the Mie solution.

The advantage of using a geometry conforming tetrahedral mesh is demonstrated by performing a simulation using a uniform cartesian mesh and a DGTD-$\mathbb{Q}_1$ method. The underlying mesh contains $200 \times 200 \times 200$ cells. The obtained solution is visualized on Fig. 5 on which one can in particular notice that the maximum value of the resonance is greatly over evaluated. Finally, performance results are given in Table 2. For each solution strategy, we partition the mesh into 4, 8 and 16 subdomains and run computations on a cluster of Intel Xeon 2.66 GHz nodes (each consisting of 8 computing cores and 32 Gb of RAM), interconnected by an Infiniband network. The parallel speedups are satisfying, in spite of a slight superiority of the DGTD-$\mathbb{P}_2$ method. There are two main reasons explaining this behavior. First, the fact that it is easier to

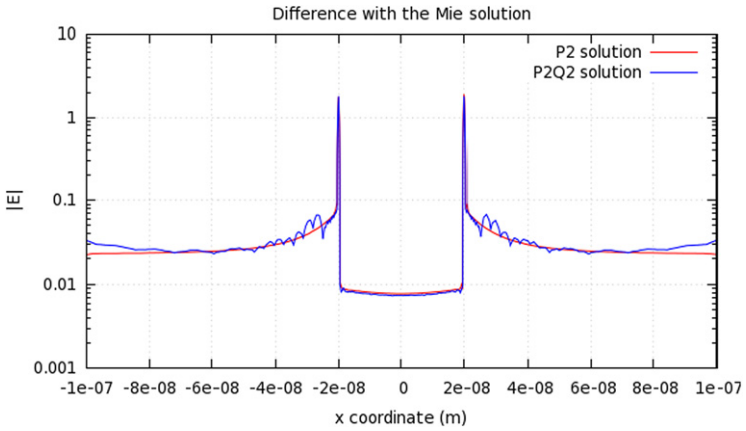

Fig. 4. 1D distribution along the *x* axis of the difference with the Mie solution of the modulus of the electric field in the Fourier domain.

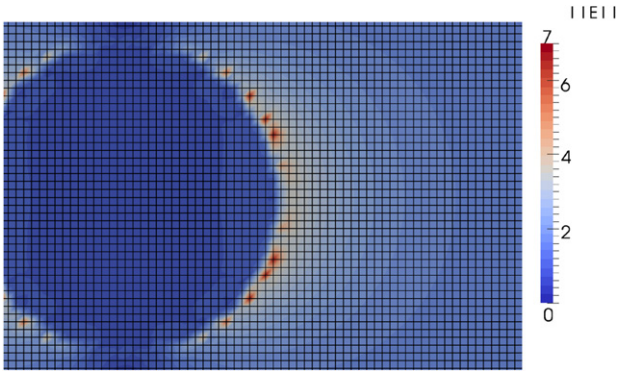

Fig. 5. Simulation of the scattering of a plane wave by a single nanosphere. Numerical illustration of the staircasing effect using the DGTD-$\mathbb{Q}_1$ solution method on a uniform cartesian mesh.

Table 2
Simulation of the scattering of a plane wave by a single nanosphere. Performance results: CPU time for 1000 iterations and parallel speedup (in parentheses).

–	Sequential	4 cores	8 cores	16 cores
DGTD-$\mathbb{P}_2$	7534 s (1.0)	1878 s (4.0)	966 s (7.8)	515 s (14.6)
DGTD-$\mathbb{P}_2\mathbb{Q}_2$	4321 s (1.0)	1179 s (3.7)	634 s (6.8)	340 s (12.7)

approach an optimal load balancing in the case of a fully tetrahedral mesh. Second, the DGTD-$\mathbb{P}_2$ method involves twice as much degrees of freedom as the DGTD-$\mathbb{P}_2\mathbb{Q}_2$ method, thus improving the ratio of computing time to communication time.

4.2. L-shaped nanospheres waveguide

In order to illustrate the benefits of using non-conforming multi-element meshes, we now consider a more challenging application in the field of optical and electronic engineering. The selected test problem involves an L-shaped waveguide inspired by [25,26]. This L-shaped waveguide is formed of seven 50 nm diameter Au spheres in vacuum, with a 75 nm center-to-center spacing while the whole computational domain consists of a 550 nm$\times$ 750 nm$\times$ 400 nm parallelepipedic domain. A Silver–Müller absorbing boundary condition is applied on the surface of this parallelepipedic domain. When excited by an optical regime source, the interest of this setting is the sub-wavelength energy guiding, from sphere to sphere, due to the surface plasmons coupling with each other. It follows that the geometry of the spheres should be correctly approximated in order to avoid non-physical energy concentration phenomena in spurious wedges of the mesh. Moreover, the vicinity of the spheres should be accurately resolved in order to capture the sub-wavelength phenomena of interest. Finally, the physical time window of the computation should be long enough for the phenomenon to settle. This test problem has been simulated using a DGTD-$\mathbb{P}_2$ method applied on a fully tetrahedral mesh and a DGTD-$\mathbb{P}_2\mathbb{Q}_2$ method applied on a non-conforming hexahedral–tetrahedral mesh. The two meshes are partially visualized on Fig. 6 and their characteristics are summarized in Table 3. The source term is a dipole localized in the tetrahedral subdomain, 75 nm away from the center of the first sphere in

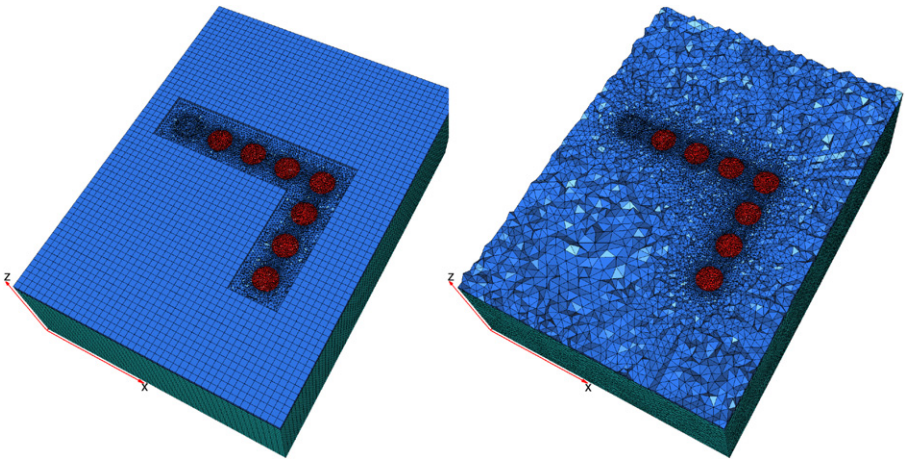

Fig. 6. Partial views of the tetrahedral and hybrid hexahedral–tetrahedral meshes used for the simulation of the L-shaped waveguide.

Table 3
Characteristics of the tetrahedral and hybrid hexahedral–tetrahedral meshes used for simulation of the L-shaped waveguide.

–	# vertices	# tetra	# hexa	# d.o.f
DGTD-$\mathbb{P}_2$	222,175	1,306,356	0	13,063,560
DGTD-$\mathbb{P}_2\mathbb{Q}_2$	211,214	706,012	81,280	9,264,660

Table 4
Simulation of an L-shaped waveguide. Performance results: CPU time to reach 1 fs and parallel speedup (in parentheses).

–	8 cores	16 cores	32 cores	64 cores	128 cores
DGTD-$\mathbb{P}_2$	11420 s (1.0)	5710 s (2.0)	2800 s (4.1)	1455 s (7.8)	762 s (15.0)
DGTD-$\mathbb{P}_2\mathbb{Q}_2$	5680 s (1.0)	2804 s (2.0)	1439 s (3.9)	848 s (6.7)	494 s (11.5)

the guide. This dipolar source amounts to imposing a current density of the form $J_x(x, y, z, t) = \delta(x - x_s, y - y_s, z - z_s)f(t)$ with $f(t) = \left(1 - e^{-(t/\alpha)^2}\right) \sin(2\pi f_c t)$ where the central frequency is $f_c = 622.65$ THz, $\gamma = 2.5 \times 10^{16}$, and $\alpha = 2.5833$ fs. The parameters of the Drude model for the Au nanospheres are $\varepsilon_\infty = 1$, $\omega_d = 6.79 \times 10^3$ THz and $\gamma_d = 2.5 \times 10^2$ THz. Time steps for these simulations are $\Delta t_{\text{hyb}} = 3.9 \times 10^{-4}$ fs and $\Delta t_{\text{tet}} = 3.7 \times 10^{-4}$ fs. Performance results are given in Table 4 for up to 128 cores, on the cluster system already used for the previous test problem. Here again, a better scalability is observed with the DGTD-$\mathbb{P}_2$ method although the DGTD-$\mathbb{P}_2\mathbb{Q}_2$ strategy remains significantly faster. Fig. 7 shows the physical results in the form of contour lines of the E_z component on the $z = 0$ plane, first, after 6.02 fs as the resonances start to settle, and second, after 34.13 fs as the phenomenon is well-established. Once more, the agreement between the two solutions is very satisfying. In fact, the contour lines of the $\mathbb{P}_2\mathbb{Q}_2$ solution appears to be smoother than the $\mathbb{P}_2$ solution, which suggests that the fully tetrahedral mesh should be even finer for a better comparison.

5. Conclusion

In this paper, we have presented a non-conforming multi-element (tetrahedra/hexahedra) DGTD method for the solution of the system of 3D Maxwell–Drude equations. This numerical methodology is based on nodal Lagrange basis-functions, centered numerical fluxes and an explicit second order leap-frog time integration scheme. It has been implemented in a distributed memory parallel framework, relying on the MPI standard and the domain partitioning based SPMD strategy. We have shown that first, the meshing flexibility in this method offers a practical interest: it allows to accurately solve the neighborhood of the scattering objects while reducing the number of degrees of freedom in the rest of the domain, thus saving computational resources, without sacrificing numerical precision. Second, the use of a non-conforming multi-element mesh does not yield a prohibitive degradation of the parallel performances as compared to a fully tetrahedral mesh methodology. Ongoing and future works include, from a modeling point of view, the extension of this numerical methodology to more general physical dispersion models (non-local models, non-linear models). From the methodological point of view, many topics remain to be explored, such as local time-stepping methods, as well as the adaptation to the use of curved-elements, $\mathbb{P}_2$ meshes, and the adaptation of the parallelization strategy in view of exploiting massively parallel systems.

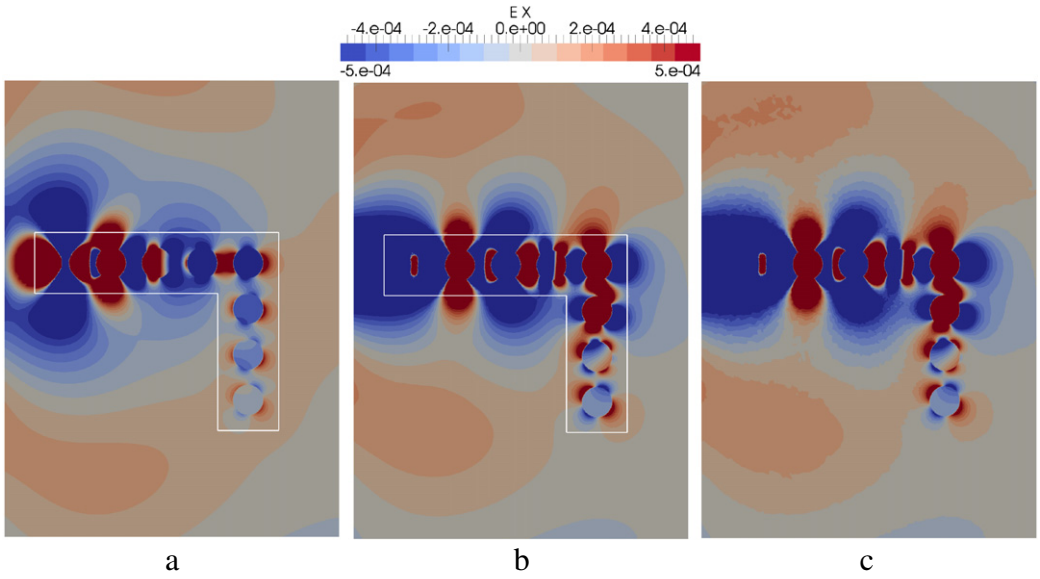

Fig. 7. Simulation of an L-shaped waveguide. X-Polarization case: E_x component of the electric field. (a): DGTD-$\mathbb{P}_2\mathbb{Q}_2$ solution at time $t = 6.02$ fs. (b): DGTD-$\mathbb{P}_2\mathbb{Q}_2$ solution at final time $t_f = 34.13$ fs. (c): DGTD-$\mathbb{P}_2$ solution at final time $t_f = 34.13$ fs.

Acknowledgments

The authors gratefully acknowledge support from Région Ile-de-France in the framework of the MIEL3D-MESHER project of the System@tic Paris-Région cluster for the doctoral thesis of Clément Durochat on one hand, and of the Direction Générale de l'Armement (DGA) which partially supports the doctoral thesis of Jonathan Viquerat.

References

[1] S. Maier, Plasmonics—Fundamentals and Applications, Springer, 2007.
[2] N.A. Mortensen, G. Toscano, S. Raza, N. Stenger, W. Yan, A.-P. Jauho, S. Xiao, M. Wubs, Nanoplasmonics beyond Ohms'law, in: D. Chigrin (Ed.), 5th International Workshop on Theoretical and Computational Nano-Photonics, TaCoNa-Photonics 2012, in: American Institute of Physics Conference Proceedings Series, vol. 1475, AIP, Bad Honnef, Germany, 2012, pp. 28–32.
[3] J. McMahon, S. Gray, G. Schat, Calculating nonlocal optical properties of structures with arbitrary shape, Phys. Rev. B 82 (2010) 035423.
[4] A. Taflove, S. Hagness, Computational Electrodynamics: The Finite-difference Time-domain Method, third ed., Artech House Publishers, 2005.
[5] P. Drude, Zur elektronentheorie der metalle, Ann. Phys. 306 (1900) 566–613.
[6] A. Vial, A.S. Grimault, D. Macias, D. Barchiesi, M.L. de la Chapelle, Improved analytical fit of gold dispersion: application to the modelling of extinction spectra with the FDTD method, Phys. Rev. B 71 (8) (2005) 085416–085422.
[7] L. Fezoui, S. Lanteri, S. Lohrengel, S. Piperno, Convergence and stability of a discontinuous Galerkin time-domain method for the 3D heterogeneous Maxwell equations on unstructured meshes, ESAIM: Math. Model. Numer. Anal. 39 (6) (2005) 1149–1176.
[8] J. Hesthaven, T. Warburton, Nodal high-order methods on unstructured grids. I. Time-domain solution of Maxwell's equations, J. Comput. Phys. 181 (1) (2002) 186–221.
[9] H. Fahs, Development of a *hp*-like discontinuous Galerkin time-domain method on non-conforming simplicial meshes for electromagnetic wave propagation, Int. J. Numer. Anal. Model. 6 (2) (2009) 193–216.
[10] H. Fahs, High-order leap-frog based biscontinuous Galerkin method for the time-domain Maxwell equations on non-conforming simplicial meshes, Numer. Math. Theory Methods Appl. 2 (3) (2009) 275–300.
[11] H. Fahs, S. Lanteri, A high-order non-conforming discontinuous Galerkin method for time-domain electromagnetics, J. Comput. Appl. Math. 234 (2010) 1088–1096.
[12] T. Cabel, J. Charles, S. Lanteri, Performance evaluation of a multi-GPU enabled finite element method for computational electromagnetics, in: 4th Workshop on UnConventional High Performance Computing 2011 (UCHPC 2011). European Conference on Parallel and Distributed Computing (Euro-Par 2011), in: Lecture Notes in Computer Sciences, vol. 7156, Springer, Bordeaux, France, 2012, pp. 355–364.
[13] E. Montseny, S. Pernet, X. Ferriéres, G. Cohen, Dissipative terms and local time-stepping improvements in a spatial high order discontinuous Galerkin scheme for the time-domain Maxwell's equations, J. Comput. Phys. 227 (14) (2008) 6795–6820.
[14] L. Moya, S. Descombes, S. Lanteri, Locally implicit time integration strategies in a discontinuous Galerkin method for Maxwell's equations, J. Sci. Comput. 56 (1) (2013) 190–218.
[15] S. Dosopoulos, J. Lee, Interconnect and lumped elements modeling in interior penalty discontinuous Galerkin time-domain methods, J. Comput. Phys. 229 (2) (2010) 8521–8536.
[16] J. Niegemann, M. König, K. Stannigel, K. Busch, Higher-order time-domain methods for the analysis of nano-photonic systems, Photonics Nanostruct. 7 (2009) 2–11.
[17] K. Stannigel, M. Koenig, J. Niegemann, K. Busch, Discontinuous Galerkin time-domain computations of metallic nanostructures, Opt. Express 17 (2009) 14934–14947.
[18] M. König, K. Busch, J. Niegemann, The discontinuous Galerkin time-domain method for Maxwell's equations with anisotropic materials, Photonics Nanostruct. Fund. Appl. 8 (4) (2010) 303–309.
[19] H. Songoro, M. Vogel, Z. Cendes, Keeping time with Maxwell's equations, IEEE Microw. 11 (2) (2010) 42–49.
[20] D. Dunavant, High degree efficient symmetrical Gaussian quadrature rules for the triangle, Int. J. Numer. Methods Eng. 21 (1985) 1129–1148.
[21] J. Viquerat, S. Lanteri, C. Scheid, Theoretical and Numerical Analysis of Local Dispersion Models Coupled to a Discontinuous Galerkin Time-domain Method for Maxwell's Equations, Tech. Rep., INRIA, 2013.

[22] C. Durochat, S. Lanteri, C. Scheid, High order non-conforming multi-element discontinuous Galerkin method for time domain electromagnetics, Appl. Math. Comput. (ISSN: 0096-3003) 224 (2013) 681–704. http://dx.doi.org/10.1016/j.amc.2013.08.069.
[23] G. Karypis, V. Kumar, A fast and high quality multilevel scheme for partitioning irregular graphs, SIAM J. Sci. Comput. 20 (1) (1998) 359–392.
[24] H. van de Hulst, Light Scattering by Small Particles, Dover, 1981.
[25] F.L. Teixeira, Time-domain finite-difference and finite-element methods for Maxwell equations in complex media, IEEE Trans. Antennas and Propagation 56 (8) (2008) 2156–2166.
[26] K.-Y. Jung, F.L. Teixeira, R.M. Reano, Au/SiO_2 nanoring plasmon waveguides at optical communication band, J. Lightwave Technol. 25 (9) (2007) 2757–2765.